受入
84-11-24
高工研図書室

EUROPEAN ORGANIZATION FOR NUCLEAR RESEARCH

CERN-EP/84-133
3 October 1984

CHARGED PARTICLE SPECTRA IN *αα* AND *αp* COLLISIONS AT THE CERN ISR

W. Bell[1], K. Braune[2,a], G. Glaesson[3,b], D. Drijard[1], M.A. Faessler[1], H.G. Fischer[1], H. Frehse[1,c], S. Garpman[3], W. Geist[1,b], C. Gruhn[4], P. Hanke[5], M. Heiden[5,b], W. Herr[5], P.G. Innocenti[1], T.J. Ketel[2,d], E.E. Kluge[5], I. Lund[3], G. Mornacchi[1], T. Nakada[5,e], I. Otterlund[3], B. Povh[2], A. Putzer[5], B. Rensch[5], E. Stenlund[3], T.J.M. Symons[4], M. Szczekowski[1], R. Szwed[2,f], O. Ullaland[1] and M. Wunsch[5]

CERN-Heidelberg-Lund Collaboration

ABSTRACT

Momenta of charged particles produced in inelastic *αα*, *αp*, and pp collisions were measured using the Split-Field-Magnet detector at the CERN Intersecting Storage Rings. Inclusive and semi-inclusive spectra are presented as a function of rapidity y, Feynman-x, and transverse momentum p_T. The inclusive y distributions agree well with predictions of the dual parton model; the highest particle densities are reached at $y \simeq 0$ and the momenta of leading protons decrease significantly for increasing total multiplicity. 'Temperatures' are equal in *αα*, *αp*, and pp interactions. The p_T distributions depend weakly on the multiplicity.

(Submitted to Zeitschrift für Physik C)

---

[1] CERN, Geneva, Switzerland.
[2] Max Planck Institut für Kernphysik, Heidelberg, Fed. Rep. Germany.
[3] Division of Cosmic and Subatomic Physics, University of Lund, Sweden.
[4] Nuclear Science Division, LBL, University of California, Berkeley, CA, USA.
[5] Institut für Hochenergiephysik der Universität, Heidelberg, Fed. Rep. Germany.
[a] Present affiliation: SLAC, Stanford, CA, USA.
[b] Present affiliation: LBL, Berkeley, CA, USA.
[c] Present affiliation: Brown Boveri, Turgi-Baden, Switzerland.
[d] Present affiliation: Natuurkundig Lab., Vrije Universiteit Amsterdam, Netherlands.
[e] Present affiliation: SIN, Villigen, Switzerland.
[f] Present affiliation: Institute of Experimental Physics, University of Warsaw, Poland.

1. INTRODUCTION

1.1 General

Theoretical predictions of a new state of matter—the quark–gluon plasma [1]—and estimates leading to the conclusions that this state can be produced in high-energy interactions of heavy nuclei have sparked a revival of interest in the study of inelastic interactions of nuclei. The successful storage of α beams in the CERN Intersecting Storage Rings (ISR) has allowed the investigation of $\alpha\alpha$ and αp collisions at the highest centre-of-mass (c.m.) energy available at accelerators.

On the one hand, such investigations with light nuclei will provide the constraints and guidelines needed for extrapolations to collisions of heavier nuclei when dedicated high-energy nucleus–nucleus colliding-beam facilities become available. On the other hand, the present measurements provide useful tests for the predictions of various models of hadron production in strong interactions, which become more and more distinguishable the higher the c.m. energy is.

The measured topological cross-sections in $\alpha\alpha$ and αp collisions have already been published [2]. In this paper inclusive and semi-inclusive momentum and rapidity distributions of charged particles are presented. The data were obtained using the Split-Field-Magnet (SFM) detector. A brief description of the detector and the experimental procedure will be given in this section. In Section 2 the fully inclusive rapidity distributions are shown and compared with predictions of several theoretical models, and the multiplicity dependence of the rapidity distributions is presented. Section 3 is devoted to the study of particle distributions in longitudinal momentum, or Feynman-x (x_F). Finally, in Section 4 the transverse momentum spectra and their multiplicity dependence are investigated.

1.2 Experimental set-up

The SFM detector [3] is a large-volume magnetic spectrometer designed to measure the momenta of charged particles over almost 4π sr. The track detector consists of banks of multiwire proportional chambers completely enclosing the intersection region, such that only high-momentum particles at small polar angles ($\theta < 7$ mrad) are lost in the beam pipes. The data were taken using a minimum bias trigger, which requires at least one track candidate in the detector, defined by a coincidence of three or more space points. The present analysis is based on 110,000 $\alpha\alpha$ and 41,000 αp inelastic events. The beam momenta were 62 GeV/c for alpha particles and 31 GeV/c for protons; thus the c.m. energies per nucleon–nucleon collision, $\sqrt{s_{NN}}$, were 31.2 GeV for $\alpha\alpha$ and 44.0 GeV for αp interactions.

1.3 Experimental procedure

The events were processed by the standard SFM reconstruction programs. The efficiency of the detector and of the reconstruction was calculated by a Monte Carlo simulation. The Monte Carlo program consists of three stages: event generator, tracking of particles through the detector to produce simulated wire hits, and reconstruction of these simulated raw data by the same program chain that was used to process real data. In the Monte Carlo procedure secondary processes such as Coulomb scattering, δ-ray production, secondary interactions, and pion and kaon decays were included. From the comparison of the generated and reconstructed events, single-track acceptance tables were produced which were then used to correct the measured inclusive distributions. The contamination by electrons from γ-conversion and by tracks coming from K^0 and Λ decays was estimated using a special Monte Carlo program. The track efficiency averaged over phase space was found to be 80–85% depending on the magnetic field setting [1 T for $\alpha\alpha$ and αp, 0.85 T for pp ($\sqrt{s} = 44$ GeV), and 0.5 T for pp ($\sqrt{s} = 30.4$ GeV)]. All inclusive spectra were acceptance-corrected and normalized to the production cross-section, σ_{prod}, which

corresponds to the total inelastic cross-section after subtracting the cross-section for nuclear breakup without particle production [2].

As mentioned, large track losses (due to the beam pipe) occur only for particles having rigidities (p/Q) close to the beam rigidity. Thus the spectra have large uncertainties for positive particles with $p/Q \gtrsim 0.7\,(p/Q)_{beam}$ and information from this region should be taken as qualitative rather than quantitative.

2. RAPIDITY DISTRIBUTIONS

2.1 Rapidity distributions of negative secondaries

In studies of inclusive distributions of charged particles as a function of the rapidity*),

$$y = 0.5 \ln [(E + p_L)/(E - p_L)], \tag{1}$$

with E and p_L being the energy and longitudinal momentum, respectively, the pion mass is generally assumed in cases where the mass of the particle is unknown. This leads to large distortions of the spectrum except for negative particles since they are predominantly pions. The inclusive rapidity distributions

$$dn/dy = (\sigma_{prod})^{-1}\, d\sigma/dy \tag{2}$$

of negative secondaries produced in $\alpha\alpha$ and αp collisions together with the corresponding distributions for pp interactions at the same $\sqrt{s_{NN}}$ are plotted in Fig. 1 for linear and logarithmic vertical scales. The solid curves correspond to the theoretical predictions discussed later.

Figure 2 shows the ratios $R_{\alpha\alpha}(y)$ between $\alpha\alpha$ and pp rapidity distributions of negative secondaries at equal values of $\sqrt{s_{NN}}$ and similarly for $R_{\alpha p}(y)$:

$$\begin{aligned} R_{\alpha\alpha}(y) &= [dn(\alpha\alpha \to h^-)/dy] / [dn(pp \to h^-)/dy] \\ R_{\alpha p}(y) &= [dn(\alpha p \to h^-)/dy] / [dn(pp \to h^-)/dy]. \end{aligned} \tag{3}$$

The ratio $R_{\alpha\alpha}(y)$ has a central plateau extended over about 4 units in y with a value of 1.66 ± 0.08 at $y = 0$ and rises steeply at the two edges. The ratio $R_{\alpha p}(y)$ shows a slightly tilted plateau with a value of 1.10 ± 0.06 at $y = 0$ and is steeply rising at the edge ($y > 0$) where the α particle has fragmented. The steep rise of the ratios for $y > 3$ is largely due to isospin effects. In the fragmentation region of an incoming proton the yield of π^+ is larger (up to a factor of 5 for $x_F > 0.8$) than the π^- yield, but for an equal mixture of incoming p and n the yields of π^- and π^+ are expected to be equal. Obviously, the comparison of $\alpha\alpha$ (αp) rapidity distributions should rather be done with average nucleon–nucleon (nucleon–proton) than with pp data because of the different initial isospins, but these data were not available.

2.2 Comparison with models

The lines drawn in Figs. 1 and 2 correspond to theoretical calculations performed within various parton models [4–6] for $\alpha\alpha$ and αp collisions. The predictions of the quark–parton model [4] and additive quark model [5] were limited to the rapidity ratio R(y) for the central rapidity region, whereas in the case of the dual parton model [6] the full rapidity spectra ($|y| < 4$) were calculated.

*) All variables are defined in the c.m. system of a nucleon–nucleon collision.

The uncertainties of the model predictions are of the order of 5–8%, mostly due to the uncertainties in the cross-section values used as parameters in those models. From Fig. 2 it is apparent that in the central rapidity region all three model predictions agree with the data. The agreement between experimental data and theoretical predictions suggests that the idea of additivity of independent parton–parton interactions works for these high-energy nuclear interactions. The quark–parton model and the dual parton model predict a slightly inclined central plateau for $R_{\alpha p}(y)$, whereas the additive quark model predicts a flat central plateau for both $\alpha\alpha$ and αp collisions. Figure 2 shows that there is evidence for a rise of $R_{\alpha p}(y)$ towards increasing y.

2.3 Baryon number flow in $\alpha\alpha$ collisions

One of the interesting problems concerning nucleus–nucleus collisions at high energy is the rapidity distribution of the leading nucleons, i.e. of the protons if only charged particles are measured [7]. As mentioned before, owing to the lack of particle identification, the proton rapidity could not be directly measured and the assumption of a pion mass leads to large distortions in the rapidity distributions of positive particles. This is illustrated by Fig. 3a, where the rapidity distribution of positive particles is plotted, assuming they are i) all pions, and ii) all protons. As one can see in Fig. 3a, the rapidity distribution changes quite drastically. Although particle identification was not available it is possible, in the special case of $\alpha\alpha$ scattering, to extract the proton rapidity spectra assuming the proton mass for both negative and positive particles and calculating the difference of the rapidity spectra between positive and negative particles. Since the rapidity spectra for negative and positive pions have to be equal, owing to an equal amount of protons and neutrons (or of up and down quarks) in the incoming α particle, their contributions cancel in the difference. Protons produced in baryon–antibaryon pairs are compensated by an equal amount of antiprotons. Therefore the difference is equal to the spectrum of non-pair-produced protons, if one neglects the expected small difference in K^+ and K^- yields. The result of such a procedure is shown in Fig. 3b where, in addition, the rapidity distribution of all positive particles is plotted. This latter was obtained by adding the rapidity distribution of negative hadrons to that of leading protons (assuming the pion mass for negative hadrons). Following the explanation in Section 1.3, the result presented in Fig. 3 should be taken as qualitative at the y edges ($|y| > 3.8$). A more quantitative study of the α-fragmentation process into p, d, t, and ^{3}He will be presented in a separate paper [8]. One can learn from Fig. 3b that the proton rapidity distribution has a peak at $y = 3.5$ from spectator protons, and attached to lower $|y|$ a shoulder from interacting protons; the distribution falls rapidly when one approaches the central rapidity region. The approximate width of the proton peak is 1.5 rapidity units (FWHM). In the range $|y| < 1$ the baryon density is expected to be small [9], but the charged particle densities are large; thus the errors of the difference are dominated by uncertainties in the acceptance of negative and positive particles.

2.4 Semi-inclusive rapidity spectra

Figure 4 shows the semi-inclusive rapidity distributions for negative secondaries emitted in $\alpha\alpha$ and pp collisions. One expects for $\alpha\alpha$ collisions that increasing the integrated multiplicity n_- is equivalent to decreasing the impact parameter or to increasing the number of nucleon–nucleon collisions per event; thus one expects an overall increase of the particle density for increasing n_-. However, at first sight the change of the distributions is similar in $\alpha\alpha$ to that in pp interactions: the distributions become narrower as the multiplicity increases. This trend has already been observed in an earlier study, for charged particles produced in pp interactions [10].

A somewhat different presentation of the dependence of dn_-/dy on the total multiplicity n_- is given in Fig. 5. In the central rapidity region (Fig. 5a) we observe a linear growth of the rapidity

density with the total multiplicity for both pp and $\alpha\alpha$ data, for negative secondaries, and, similarly, for positive particles (Fig. 5d). The $\alpha\alpha$ data show the same linear rise as the pp data. At large multiplicity, up to 5 times more particles are produced (on an average) per rapidity unit compared with the overall sample (Fig. 1). In the intermediate y region, $1 < |y| < 3$ (Fig. 5b), the particle density in $\alpha\alpha$ and pp collisions still increases approximately linearly with n_-. Here the growth of particle density with n_- is faster in the case of $\alpha\alpha$ than pp collisions. The contrast manifests itself even more strongly in the fragmentation region, $3 < |y| < 6$ (Fig. 5c), where almost no increase of particle density is seen in the pp case.

3. FEYNMAN x_F DISTRIBUTIONS

3.1 Inclusive and semi-inclusive x_F distributions of charged hadrons

In Fig. 6 the x_F distributions dn/dx_F of positive and negative particles are compared for $\alpha\alpha$, αp, and pp interactions. Since the lack of particle identification excludes a precise determination of the particle energy, we show here dn/dx_F instead of the invariant distribution. We also want to recall that

$$x_F = 2p_L/\sqrt{s_{NN}} \tag{4}$$

being defined with respect to the c.m. energy $\sqrt{s_{NN}}$ per nucleon–nucleon collision, values of $|x_F|$ as large as 4 are kinematically allowed (on the α side for αp, and on both sides for $\alpha\alpha$). Once again, owing to the loss of particles near the beam rigidity the spectra of positive particles should be considered more as qualitative for $x_F > 0.7$ along the direction of the incoming proton (for αp and pp) and for $x_F > 1.4$ along the α beam direction. In the case of αp interactions, positive x_F correspond to the hemisphere where the α particle fragmented ('α side'). In the pp and $\alpha\alpha$ case the x_F distributions are of course symmetric. The comparison of αp and pp data (Figs. 6 a and b) shows that on the 'α side' the density of both negative and positive particles are larger for αp interactions over the full x_F range, whereas at the 'p-side' the densities are very close. In the positive spectra one sees peaks around $x_F = 1$ and $x_F = 2$ at the 'α side' which are due to non-interacting (spectator) or quasi-diffractively scattered protons and deuterons, respectively. (Quasi-diffractive means elastic- or inelastic-diffractive on a bound nucleon or fragment). At the 'p side' the enhancements at $x_F = 1$ correspond to the diffractive proton peak. The comparison between x_F spectra for $\alpha\alpha$ and pp collisions is presented in Figs. 6c and d. Features similar to those observed for the 'α side' in the αp spectra are seen for both hemispheres in the case of $\alpha\alpha$ collisions.

The invariant semi-inclusive x_F distributions of negative particles produced in $\alpha\alpha$ collisions,

$$F(x_F) = \int 2E/(\pi\sqrt{s})\,[(1/\sigma_n)(d^2\sigma_n/dx d^2p_T)]d^2p_T\,, \tag{5}$$

are shown in Fig. 7 and compared with pp data ($\sqrt{s} = 30.4$ GeV) for different ranges of the charged track multiplicity N_c in the central rapidity region $|y| < 2$; the choice of the multiplicity bins used in Fig. 7 and in some of the following figures is illustrated in Fig. 8. The bins are $N_c = 0$; $1 \leq N_c \leq 2$; $3 \leq N_c \leq 5 \leq$; $6 \leq N_c \leq 10$; $11 \leq N_c \leq 17$; $18 \leq N_c$.

The information contained in Fig. 7 overlaps with that in Figs. 3 and 4, apart from the different windows chosen for the integrated multiplicity (N_c is approximately equal to $2n_-$ and the y window for N_c, $|y| < 2$, corresponds approximately to an x_F window $|x_F| < 0.1$). However, in this representation of the data, using x_F instead of y, the high-y region is more emphasized ($x_F > 0.3$ corresponds to about $y > 3.4$).

The spectra in Fig. 7 were shifted up, by applying a factor 2^{i-1} for subsequent bins i of the multiplicity N_c. Apparently, above $x_F > 0.3$ the particle density remains almost constant for increasing N_c (and $i > 1$), in the case of $\alpha\alpha$ as in the case of pp collisions. In both cases the particle

density increases strongly in the region $x_F < 0.3$. The distributions fall more rapidly in pp interactions, as expected from isospin considerations, see Section 2.1. Single-exponential functions were fitted to the distributions in the range $0.3 < x_F < 0.8$. The fitted parameters are listed in Table 1.

3.2 p_L or x_F spectra of protons in *aa* interactions

If we calculate the difference $dn_+/dp_L - dn_-/dp_L$ between positive and negative particles in *aa* interactions we obtain, for the reasons explained in Section 2.3, essentially the p_L distribution of protons shown in Fig. 9a as a function of the absolute values $|p_L|$. This distribution measures directly the momentum loss of the nucleons (or the 'inelasticity', 'transparency', or 'stopping power') in *aa* interactions. This figure shows a peak at $p_L \simeq 15$ GeV/c ($x_F \simeq 1$) ascribed above as being due to spectator and quasi-diffractive protons. For $p_L > 10$ GeV/c we have not used the acceptance calculated by the Monte Carlo simulation which was described in Section 1.3, since this acceptance was not considered as reliable in the region close to the edges of the chambers surrounding the beam pipes. Rather an empirical acceptance table was used. This was obtained by comparing pp data ($\sqrt{s_{NN}} = 63$ GeV) taken with the SFM detector (the magnetic field being the same as for the *aa* measurement) with all other existing data at high energy; for $p_L < 10$ GeV/c the Monte Carlo and empirical acceptances agree reasonably well, whereas for p_L around 15 GeV/c the latter is lower than the Monte Carlo acceptance by about 30%. The acceptance for protons is only poorly known at $p_T < 0.15$ GeV/c owing to lack of data for our empirical acceptance. The procedure to obtain this empirical acceptance is described in detail in Ref. [8]. The almost homogeneous distribution for $p_L < 12$ GeV/c has to be compared with the (also flat) x_F distribution of protons measured in pp interactions [11].

It is also interesting to investigate how this distribution changes if one increases the multiplicity N_c of particles produced in the event. A priori one expects a decrease in the number of spectator or quasi-diffractive protons, and an increase in the number of inelastic protons, together with a shift of the latter to lower p_L or x_F. The latter trend is clearly seen in the data of Fig. 9 b but the decrease of spectator protons only starts at the highest multiplicity bin; below that the content of the peak is almost constant. The total number of protons (the integral over the p_L distribution), which is given at the right edge of the figure, reaches a value close to 4 only at the highest multiplicity bin. Hence one has to conclude that at lower multiplicity a fraction of the protons is 'hidden'. A plausible explanation is that at low multiplicity often larger fragments of the incoming α, such as d, t, or ^{3}He are formed. Owing to the complete lack of acceptance for tracks with polar angles < 7 mrad, caused by the beam pipes, most heavy fragments are not detected—the lower p_T cut is 0.2, 0.3, 0.3 GeV/c for d, t, ^{3}He, respectively.

Thus we believe that Fig. 9 provides useful information on the inelasticity and change of inelasticity as a function of multiplicity, for the protons involved in the interaction. Moreover the correlation between missing protons and the number of produced central tracks N_c contains implicit information on the correlation between the emission of heavy fragments and the impact parameter of the interaction.

4. TRANSVERSE MOMENTUM SPECTRA

4.1 Average transverse momentum and temperature of the collision

Figure 10 gives invariant cross-sections for negative and positive particles produced in *aa* and *ap* collisions as a function of p_T in the central rapidity region, $|y| < 1$. Assuming a thermal distribution for particles with small transverse momenta, we fitted the following expression to the experimental distributions [12]:

$$f(p_T; A, B, T, p_0, n) = Ed^3\sigma/dp^3 = A\,\theta(p_1 - p_T)\left[\sum_i N_i\sqrt{(p_T^2 + m_i^2)}\sum_\ell (\pm 1)^{\ell+1}\, K_1(\ell\sqrt{(p_T^2 + m_i^2)}/T)\right]$$
$$+ B\,\theta(p_T - p_1)\,[p_0/(_T + p_0)]^n, \qquad (6)$$

where the index i represents the particle species (π, K, p), the index ℓ runs from 1 to ∞, $\theta(x)$ is the step function, and K_1 is a modified Bessel function of the second kind; $p_1 = 0.8$ GeV/c and $N_\pi : N_K : N_p = 15:2:1$. For fermions (bosons) the $-$ (+) sign has to be used following the sum over ℓ in formula (6). For further explanations of this expression see Ref. [12].

Using formula (6), the average transverse momentum can be explicitly calculated [12]:

$$\langle p_T\rangle = \int p_T f(p_T)dp_T^2 / \int f(p_T)dp_T^2. \qquad (7)$$

Estimating $\langle p_T\rangle$ by fitting formula (6) to the data has an advantage compared to the standard calculation of the average

$$\langle p_T\rangle = \int_0^\infty p_T(dn/dp_T)dp_T / \int_0^\infty (dn/dp_T)dp_T, \qquad (8)$$

because it provides an extrapolation to the very low p_T ($p_T < 0.2$ GeV/c), where normally the experimental uncertainties are large.

We have fitted expression (6) to the experimental cross-sections in Fig. 9 within the transverse momentum range $0.3 < p_T < 2.0$. The results are presented in Table 2. For comparison we have included results obtained in the same way for pp collisions at corresponding c.m. energies. The numbers in brackets correspond to fits done with the formula most often used in the literature:

$$E\,d^3\sigma/dp^3 = A\exp(-p_T/T) \qquad (9)$$

and

$$\langle p_T\rangle = 2T,$$

which may bias the value of the temperature obtained and subsequently $\langle p_T\rangle$ [12]. The errors are statistical only; the estimated systematic errors are of the order of 4%. As one can see from Table 2, the temperatures or average transverse momenta in $\alpha\alpha$ and αp collisions are close to those measured in pp collisions at the corresponding c.m. energies.

4.2 Multiplicity dependence of the transverse momentum

Recently published $p\bar{p}$ collider data [13], which showed a significant rise of $\langle p_T\rangle$ as the particle density in the central rapidity region increases, triggered exciting speculations about the possible sources of such an effect [14]. The existence of a similar although weaker effect was later on reported for pp data at the highest ISR energies [15]. It was also observed that the effect is enhanced when one calculates $\langle p_T\rangle$ from a truncated distribution, for instance applying a lower p_T cut of 0.3 GeV/c:

$$\langle p_T\rangle_{cut} = \int_{0.3}^\infty p_T(dn/dp_T)dp_T \Big/ \int_{0.3}^\infty (dn/dp_T)dp_T. \qquad (10)$$

Figure 11 shows the $\langle p_T\rangle$ dependence on the multiplicity N_c in the central region $|y| < 2$ for $\alpha\alpha$, αp, and pp collisions. Both $\alpha\alpha$ and αp data show the same weak rise as a function of n as the pp data at $\sqrt{s} = 63$ GeV. In order to display the change of the $\langle p_T\rangle$ distribution which causes the small increase of $\langle p_T\rangle$ we have plotted, in Fig. 12, normalized semi-inclusive p_T distributions, dn/dp_T, of

charged particles produced in $\alpha\alpha$ and pp interactions for the central rapidity region $|y| < 2$. The distributions are shown for different bins of the multiplicity $n = N_c$*) and are normalized to the fully inclusive distribution:

$$R_n(p_T) = (n^{-1}\, dn/dp_T)_n / (\langle n\rangle^{-1} \langle dn/dp_T\rangle). \tag{11}$$

It is easy to see that in such a case all acceptance corrections which do not depend on the multiplicity cancel out. For comparison we have used pp data at $\sqrt{s} = 63$ GeV/c because they have the largest statistics, a multiplicity distribution which does not differ much from that for $\alpha\alpha$ (this may be relevant if there are multiplicity-dependent acceptance effects) and, furthermore, the magnetic field setting was the same. The shape of the function $R_n(p_T)$ changes with p_T and multiplicity; for low-multiplicity events a bump is seen for p_T around 0.4 GeV/c, whereas at large multiplicity a dip is seen in the same p_T range. These changes indicate a widening of the dn/dp_T distributions for increasing n. The distribution becomes flatter at $p_T > \simeq 0.4$ GeV/c [where $R_n(p_T) > 1$ for increasing n] but also rises at low p_T ($p_T < 0.4$). This kind of change also explains the fact that experimental cuts in the p_T spectrum strongly influence the multiplicity dependence of $\langle p_T\rangle$. The ratios $R_n(p_T)$ for αp (not shown here) look very similar to those presented for $\alpha\alpha$ and pp.

4.3 Transverse momentum distribution of protons at $x_F \approx 1$

The fully inclusive p_T^2 distribution of protons in the range $13 < p_L < 17$ GeV/c is shown in Fig. 13 for $\alpha\alpha$ collisions. No significant dependence of this distribution on N_c was observed for the range of N_c bins used previously. Describing the p_T^2 distribution by a sum of exponentials $\Sigma_i A_i \exp(-bp_T^2)$, at least three terms are needed to obtain a good fit ($\chi^2 = 1.2$/d.o.f.). The fitted function is shown in the figure and the fitted parameters are

$$\begin{aligned} A_1 &= 33.6 \pm 2.7, & b_1 &= -63.0 \pm 4.0, \\ A_2 &= 2.9 \pm 0.2, & b_2 &= -10.8 \pm 0.6, \\ A_3 &= 0.21 \pm 0.04, & b_3 &= -2.7 \pm 0.2. \end{aligned}$$

Also shown in the figure is the p_T^2 distribution of protons for the case of a special trigger which vetoed on any created charged particle and required at least one high-momentum track in each forward cone [8]. The distribution corresponding to this 'quasi-elastic' trigger can be described by a single exponential with a slope equal to that for pp elastic scattering. Thus the p_T^2 distribution for the inelastic trigger illustrates that the peak at $x_F = 1$ in $\alpha\alpha$ collisions contains most likely three components: true spectator protons with a very steep slope, quasi-elastically scattered protons with a slope around $-10\,(\mathrm{GeV/c})^{-2}$, and inelastic protons with a flatter slope.

5. CONCLUSIONS

We have studied the characteristic features of inclusive and semi-inclusive spectra of charged particles produced in $\alpha\alpha$ and αp interactions as a function of y, x_F or p_L, and p_T.

The rapidity distribution ratios, $R_{\alpha\alpha}(y \simeq 0) = 1.66 \pm 0.08$ and $R_{\alpha p}(y \simeq 0) = 1.10 \pm 0.06$, are in good agreement with predictions of theoretical models which assume additivity of independent parton–parton interactions.

*) In the following, n stands for N_c.

The proton density as a function of rapidity was extracted from the data. It peaks around $|y| = 3.5$ and is close to zero for $|y| < 1$.

The study of semi-inclusive rapidity distributions shows that the highest particle densities are reached in the central rapidity region. This suggests the central rapidity region as the most promising region when looking for exotic phenomena in nucleus–nucleus collisions, i.e. phenomena connected with high local energy or hadron densities.

The x_F distributions for π^- in aa collisions and, on the 'a-side', in ap collisions are flatter than those observed in pp collisions at the same $\sqrt{s_{NN}}$. For $x_F > 0.3$ the dependence on multiplicity is weak.

For increasing multiplicity, the x_F distribution of protons in aa collisions exhibits an increasing involvement of individual nucleons in the interaction and an increasing inelasticity (shift to lower x_F).

The extracted temperatures of aa and ap collisions are close to those observed in pp collisions at the same $\sqrt{s_{NN}}$. The p_T spectra change in a peculiar way with increasing multiplicity but the changes are similar for aa, ap, and pp collisions.

Acknowledgements

We wish to thank W.Q. Chao, H.J. Pirner, L. Leśniak and A. Capella for providing their calculations, and the PS and ISR operations crew for their outstanding efforts during the a runs. One of us (M.A.F.) wishes to thank the Deutsche Forschungsgemeinschaft for a Heisenberg grant. The Lund group gratefully acknowledges financial support from the Swedish Natural Science Research Council.

REFERENCES

[1] Proc. Workshop on Quark Matter Formation and Heavy Ion Collisions, Bielefeld (FRG), 10–14 May, 1982 (eds. M. Jacob and H. Satz), (World Scientific, Singapore, 1982).
M. Jacob and J. Tran Thanh Van (eds.), Phys. Rep. **88,** 325 (1982).

[2] W. Bell et al., Phys. Lett. **128B,** 349 (1982).

[3] R. Bouclier et al., Nucl. Instrum. Methods **115,** 235 (1974).
R. Bouclier et al., Nucl. Instrum. Methods **125,** 19 (1975).
M. Della Negra et al., Nucl. Phys. **B128,** 1 (1977).
W. Bell et al., Nucl. Instrum. Methods **156,** 111 (1978).

[4] S.J. Brodsky et al., Phys. Rev. Lett. **39,** 1120 (1977).

[5] A. Białas et al., Z. Phys. **C13,** 147 (1982).
L. Leśniak, private communication.

[6] A. Capella et al., Phys. Lett. **108B,** 347 (1982).
A. Capella, private communication.

[7] W. Busza and A.S. Goldhaber, Phys. Lett. **139B,** 235 (1984).

[8] W. Bell et al., preprint CERN-EP/84–131 (1984), submitted to Nucl. Phys.

[9] B. Alper et al., Nucl. Phys. **B100,** 237 (1975).

[10] W. Thomé et al., Nucl. Phys. **B129,** 365 (1977).

[11] F.C. Erné, Phys. Lett. **49B,** 356 (1974).

[12] R. Hagedorn, preprint CERN/TH. 3684 (1983).

[13] G. Arnison et al., Phys. Lett. **118B,** 167 (1982).

[14] L. Van Hove, Phys. Lett. **118B,** 138 (1982).

[15] A. Breakstone et al., Phys. Lett. **132B,** 463 (1983).

Table 1

Results from fitting exponential functions e^{a+bx_F} to the distributions $F(x_F)$, defined in Eq. (5), of negative particles produced in the range $0.3 < x_F < 0.9$

Multiplicity bin	aa ($\sqrt{s_{NN}} = 31.2$ GeV)		pp ($\sqrt{s} = 30.4$ GeV)	
	a	b	a	b
All N_c	-0.14 ± 0.04	-5.5 ± 0.1	-0.52 ± 0.11	-7.7 ± 0.3
$N_c = 0$	-0.35 ± 0.14	-4.8 ± 0.3	-0.66 ± 0.29	-7.6 ± 0.7
$1 \leq N_c \leq 2$	-0.31 ± 0.09	-5.6 ± 0.2	-0.37 ± 0.20	-8.0 ± 0.5
$3 \leq N_c \leq 5$	-0.33 ± 0.07	-5.4 ± 0.2	-0.44 ± 0.18	-7.7 ± 0.4
$6 \leq N_c \leq 10$	0.02 ± 0.06	-5.9 ± 0.1	-0.66 ± 0.32	-7.5 ± 0.8
$11 \leq N_c \leq 17$	0.26 ± 0.07	-6.1 ± 0.2		
$N_c \geq 18$	0.39 ± 0.17	-6.4 ± 0.4		

Table 2

Temperature T as obtained by fitting expression (6) to data, and corresponding $\langle p_T \rangle$ [Eq. (7)]. Numbers in brackets were obtained using Eq. (9).

	Negative tracks		Positive tracks	
	T [MeV]	$\langle p_T \rangle$ [MeV/c]	T [MeV]	$\langle p_T \rangle$ [MeV/c]
aa ($\sqrt{s_{NN}} = 31.2$ GeV)	145 ± 1	363 ± 2	149 ± 1	381 ± 2
	(178 ± 1)	(356 ± 2)	(191 ± 1)	(381 ± 2)
ap ($\sqrt{s_{NN}} = 44.0$ GeV)	143 ± 1	357 ± 2	154 ± 1	386 ± 2
	(174 ± 1)	(349 ± 2)	(190 ± 1)	(380 ± 2)
pp ($\sqrt{s} = 30.4$ GeV)	147 ± 1	364 ± 2	149 ± 1	367 ± 2
	(177 ± 1)	(353 ± 2)	(179 ± 1)	(358 ± 2)
pp ($\sqrt{s} = 44$ GeV)	145 ± 1	366 ± 2	147 ± 1	369 ± 2
	(180 ± 1)	(360 ± 2)	(182 ± 1)	(365 ± 2)

Figure captions

Fig. 1 : Rapidity distributions for negative hadrons produced in αp and $\alpha\alpha$ (full circles) and pp (open circles) collisions. The solid lines correspond to theoretical predictions of Capella et al. [6] as discussed in the text. b) and d) contain the same data as a) and c), but have a logarithmic vertical scale.

Fig. 2 : Ratio of the rapidity distributions for negative hadrons produced in $\alpha\alpha$ and pp (full circles), and αp and pp (open circles) interactions [see definition (3) in text]. The dashed, dotted, and continuous lines represent theoretical predictions [4–6].

Fig. 3 : a) Rapidity distribution of positive particles produced in $\alpha\alpha$ interactions with different mass assignments: i) π mass, ii) p mass.
b) Rapidity distributions of positive particles produced in $\alpha\alpha$ interactions evaluated with proper mass assignments: i) only protons, ii) all positive particles.

Fig. 4 : Multiplicity dependence of the rapidity distributions of negative particles in a) pp ($\sqrt{s} = 30.4$ GeV) and b) $\alpha\alpha$ ($\sqrt{s_{NN}} = 31.2$ GeV) interactions.

Fig. 5 : Dependence of the rapidity density in three different rapidity regions, a) $|y| < 1$, b) $1 < |y| < 3$, c) $3 < |y| < 6$, on the total multiplicity, for negative tracks produced in $\alpha\alpha$ and pp interactions; d) the corresponding dependence for positive tracks, $|y| < 1$.

Fig. 6 : The x_F distributions (a, c) of negative and (b, d) of positive hadrons produced (c, d) in $\alpha\alpha$ and (a, b) in αp interactions, compared with those produced in pp interactions at corresponding c.m. energy.

Fig. 7 : The semi-inclusive invariant x_F distributions of negative particles produced in $\alpha\alpha$ interactions for six different ranges of the multiplicity N_c for a) $\alpha\alpha$ collisions, $\sqrt{s_{NN}} = 31.2$; b) pp collisions, $\sqrt{s} = 30.4$ GeV; see text and Fig. 8 for the chosen N_c bins. The distributions are shifted up by factors 2^{i-1} for the i^{th} bin. The lines represent single exponential functions fitted to the data at large x_F; the fitted parameters are given in Table 1.

Fig. 8 : Frequency of events as a function of the charged vertex track multiplicity in the central rapidity region $|y| < 2$ for a) $\alpha\alpha$ collisions, $\sqrt{s_{NN}} = 31.2$ GeV; b) pp collisions, $\sqrt{s} = 30.4$ GeV.

Fig. 9 : The distribution, $dn_+/dp_L - dn_-/dp_L$, normalized per event, of the positive excess particles (protons) in $\alpha\alpha$ collisions: a) fully inclusive; b) for several multiplicity bins; the spectra are shifted by units of 0.1 for increasing multiplicity. The integrals over the distributions (i.e. the observed total charge Q) are shown on the right edge.

Fig. 10 : The invariant inclusive cross-section as a function of p_T for negative and positive particles produced in $\alpha\alpha$ and αp collisions in the central rapidity region $|y| < 1$.

Fig. 11 : Average $\langle p_T \rangle$ as a function of multiplicity in the central rapidity region for $\alpha\alpha$, αp, and pp interactions.

Fig. 12 : Normalized ratio of the transverse momentum distributions for different multiplicity bins, see definition (11), for $\alpha\alpha$ ($\sqrt{s_{NN}} = 31.2$ GeV) and pp ($\sqrt{s} = 63$ GeV).

Fig. 13 : Inclusive distribution dn/dp_T^2 (normalized per event) of positive excess particles in the range $13 < p_L < 17$ GeV/c for a) inelastic $\alpha\alpha$ interactions, b) quasi-elastic $\alpha\alpha$ interactions [8] ($\sqrt{s_{NN}} = 31.2$ GeV).

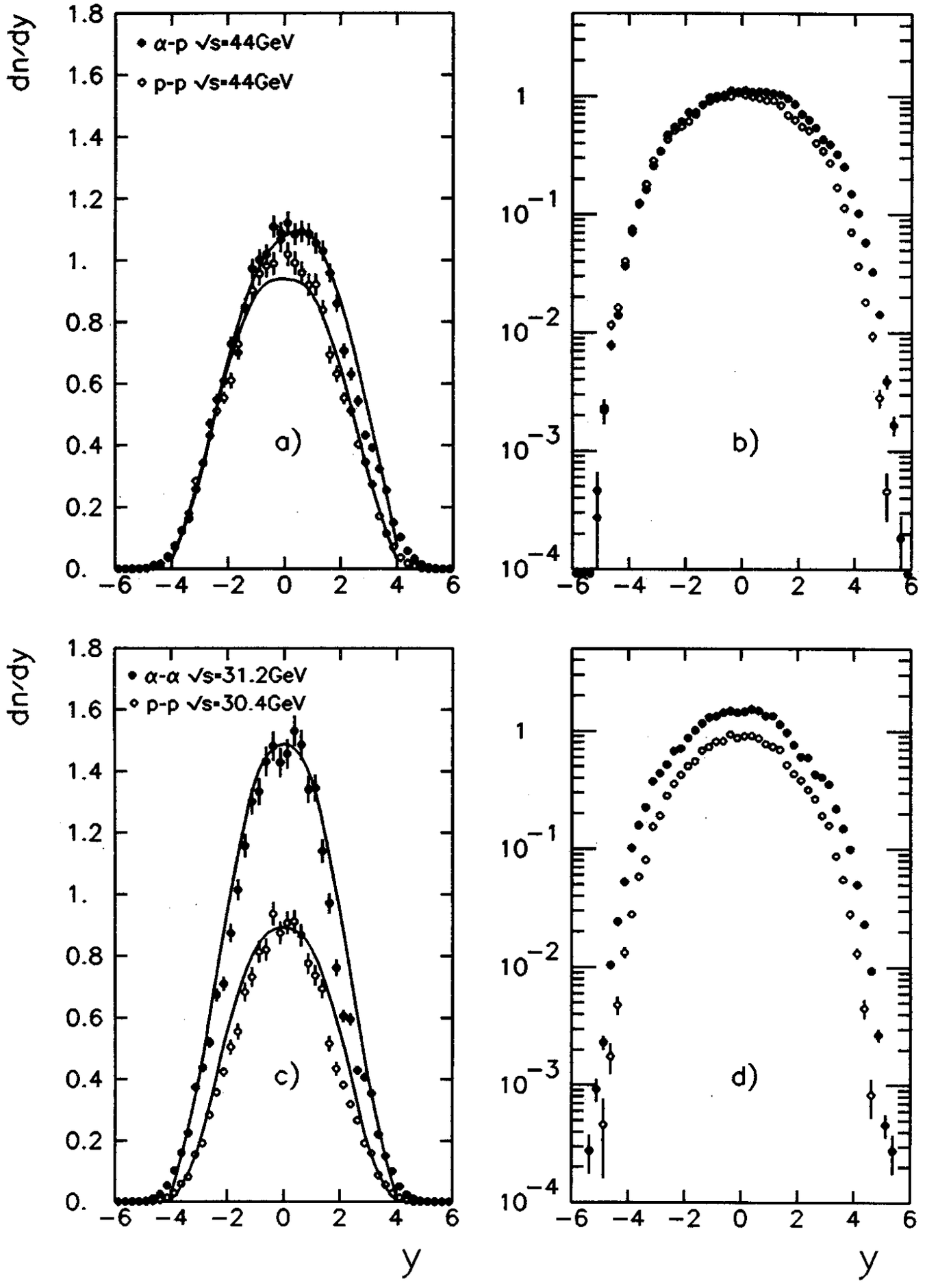

Fig. 1

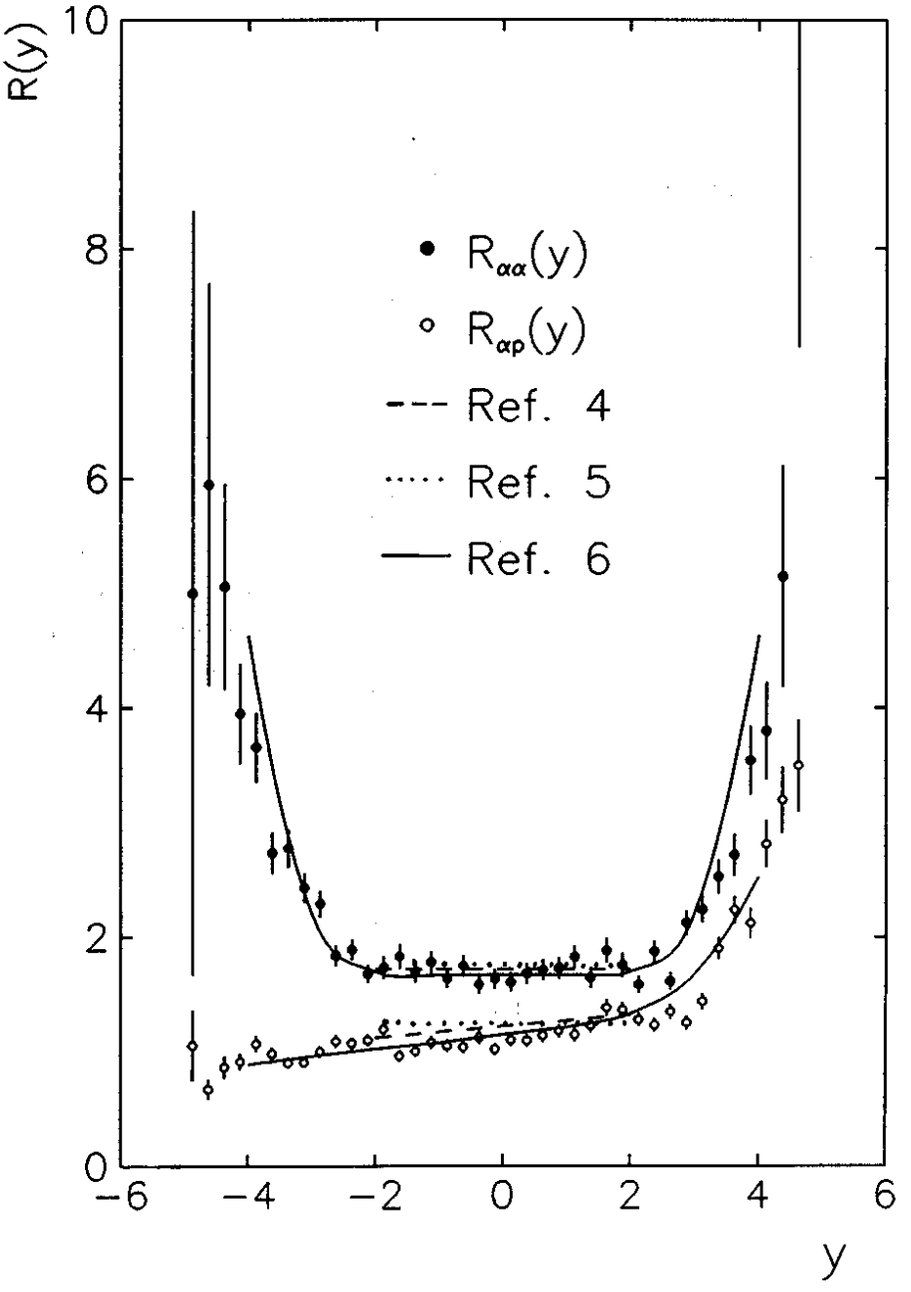

Fig. 2

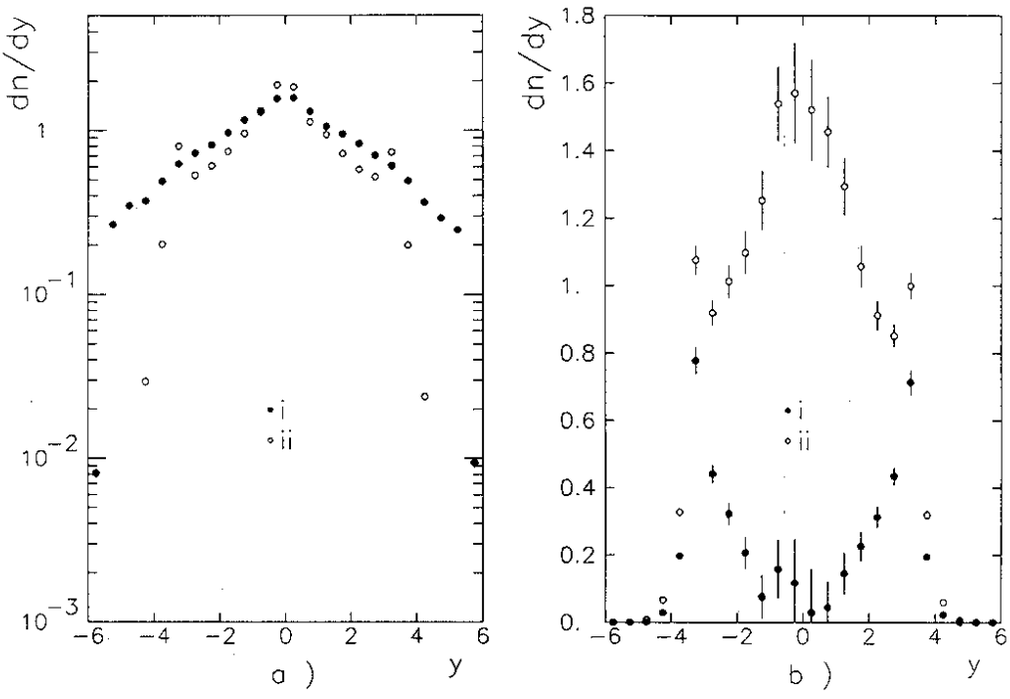
dn/dy
1
10^{-1}
10^{-2}
10^{-3}
−6 −4 −2 0 2 4 6
y
a)
• i
◦ ii
dn/dy
1.8
1.6
1.4
1.2
1.
0.8
0.6
0.4
0.2
0.
−6 −4 −2 0 2 4 6
y
b)
• i
◦ ii

Fig. 3

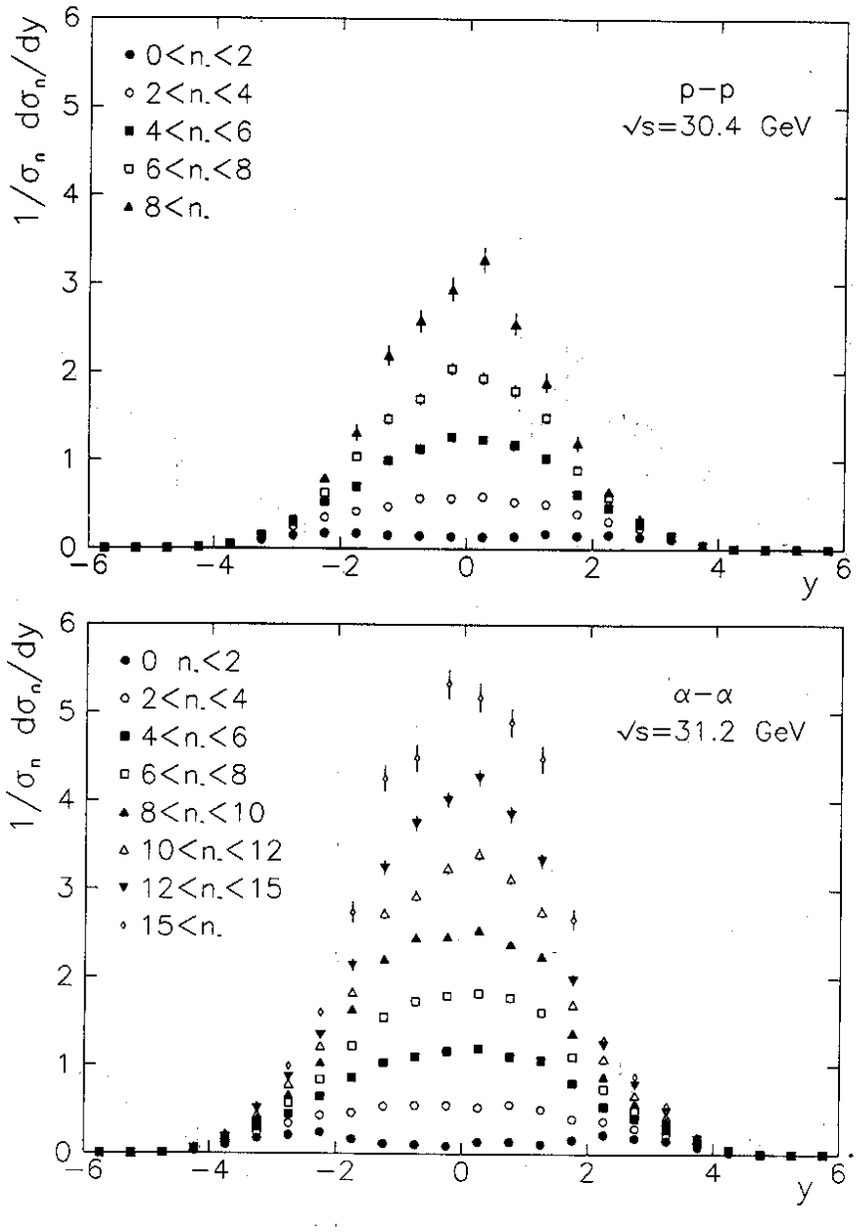
1/σn dσn/dy
0<n.<2
2<n.<4
4<n.<6
6<n.<8
8<n.
p−p
√s=30.4 GeV
y
a)
1/σn dσn/dy
0 n.<2
2<n.<4
4<n.<6
6<n.<8
8<n.<10
10<n.<12
12<n.<15
15<n.
α−α
√s=31.2 GeV
y
b)

Fig. 4

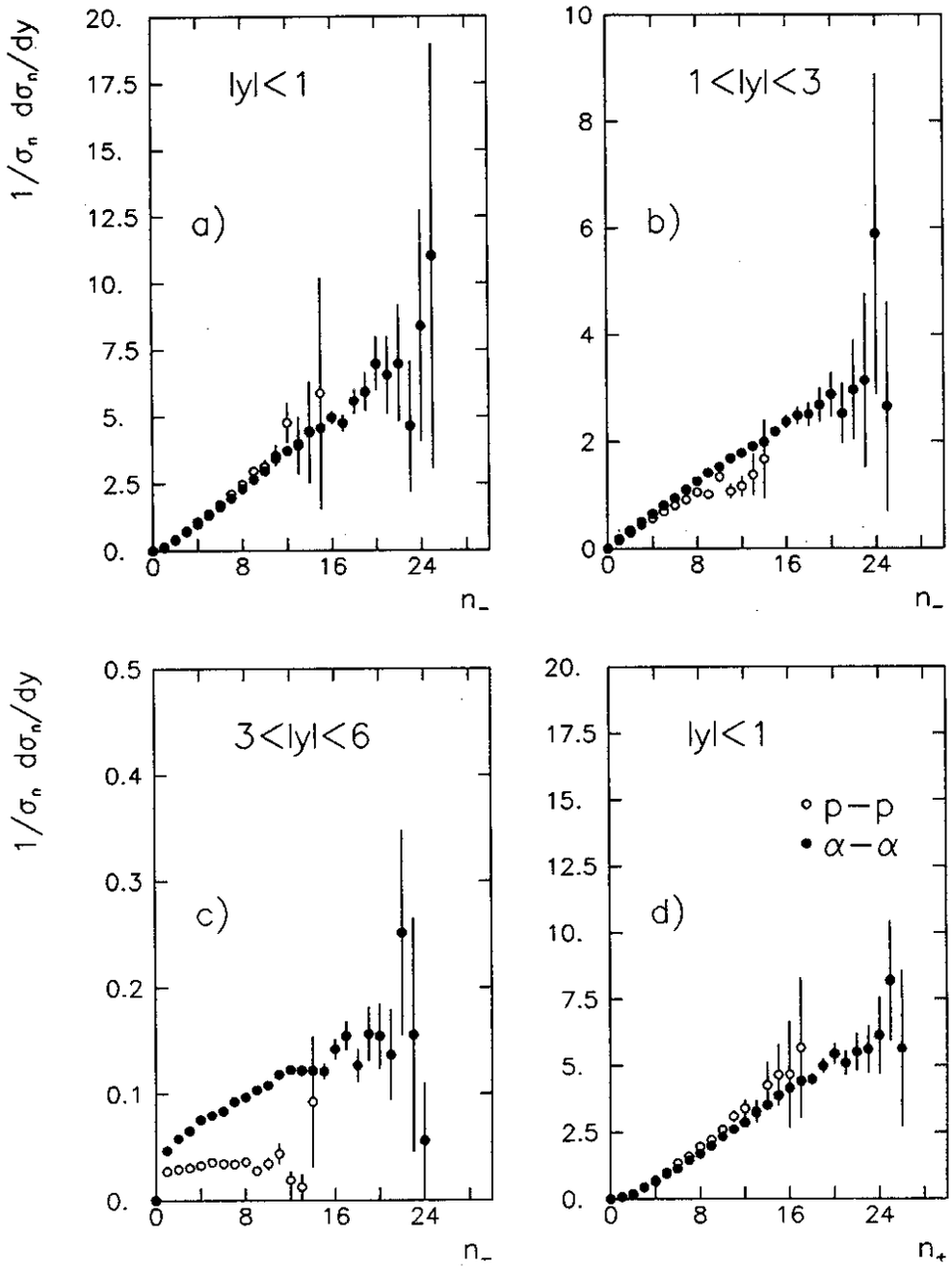

Fig. 5

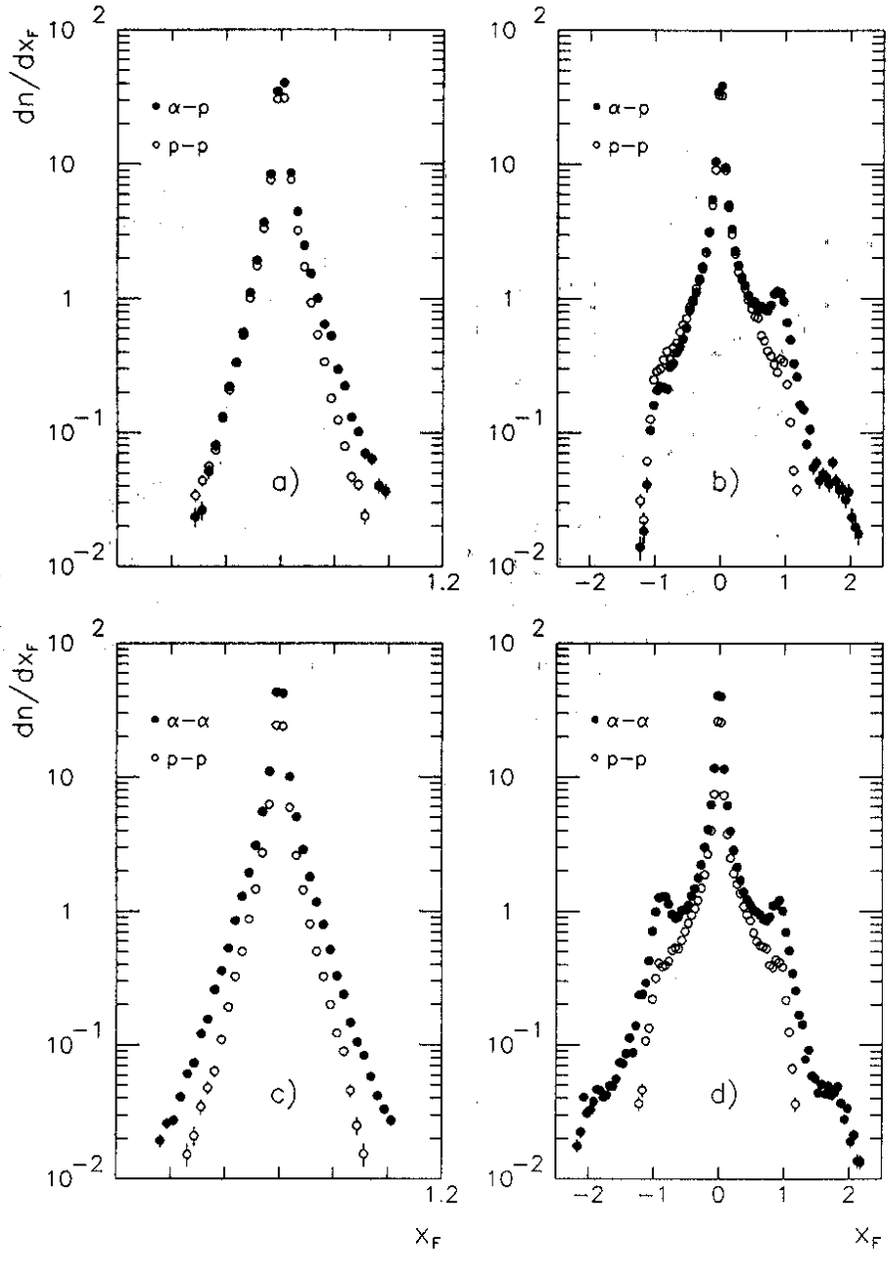

Fig. 6

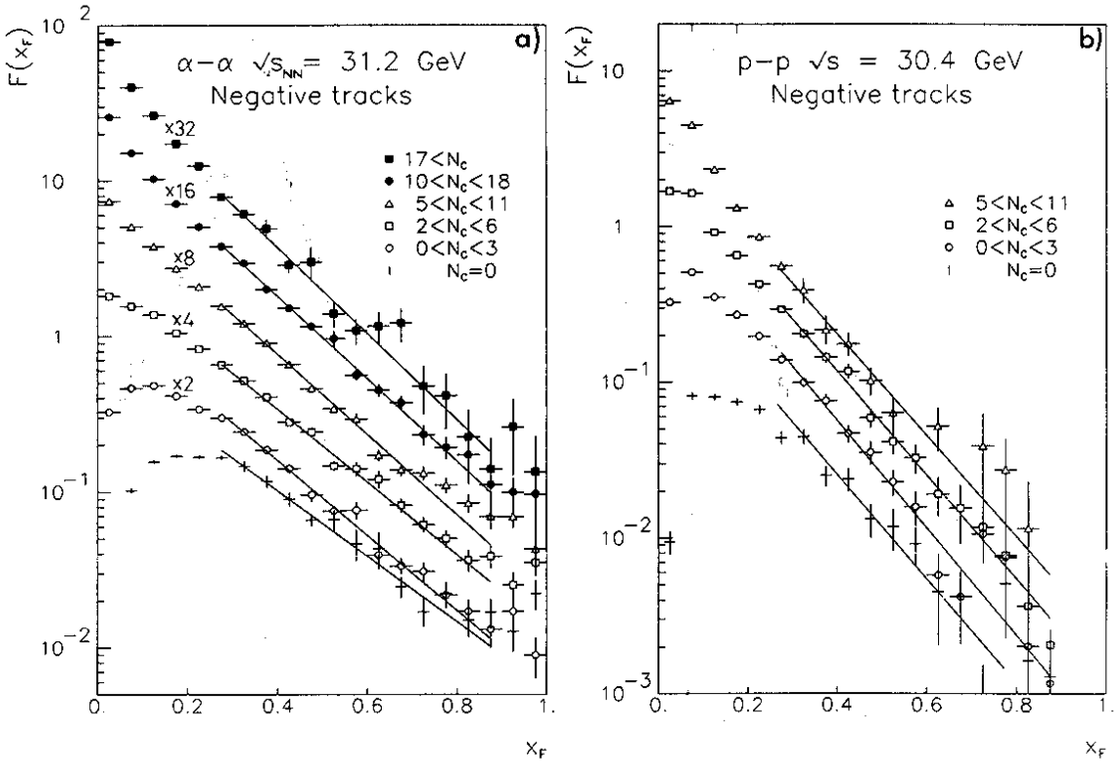
a)
α−α √s_NN = 31.2 GeV
Negative tracks
x32
x16
x8
x4
x2
17<N_c
10<N_c<18
5<N_c<11
2<N_c<6
0<N_c<3
N_c=0
F(x_F)
x_F
b)
p−p √s = 30.4 GeV
Negative tracks
5<N_c<11
2<N_c<6
0<N_c<3
N_c=0
F(x_F)
x_F

Fig. 7

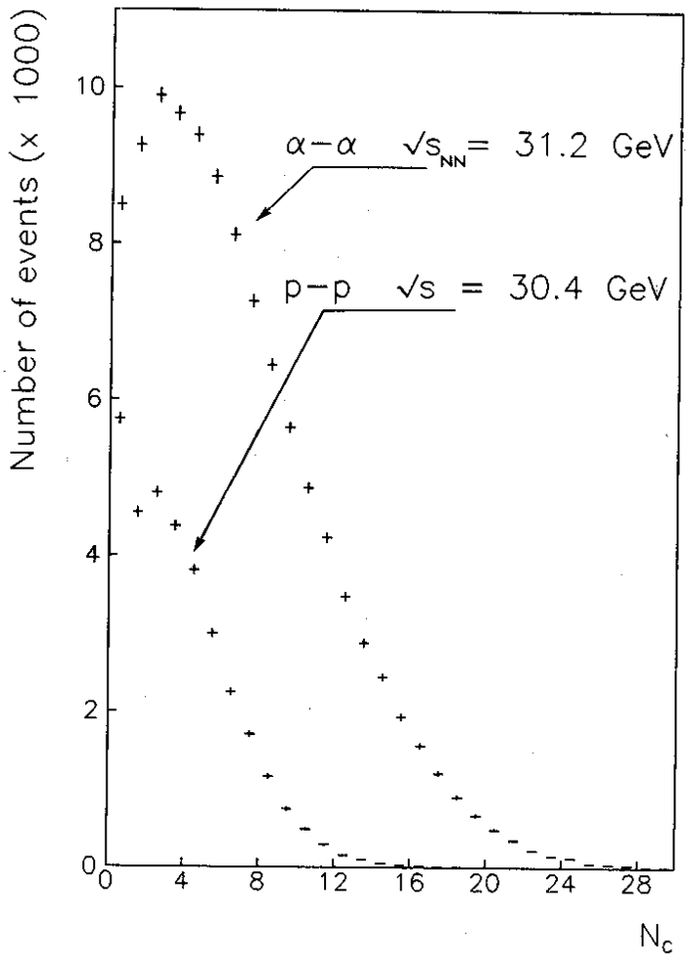
Number of events (x 1000)
10
8
6
4
2
0
0
4
8
12
16
20
24
28
N_c
α−α $\sqrt{s_{NN}}$ = 31.2 GeV
p−p $\sqrt{s}$ = 30.4 GeV

Fig. 8

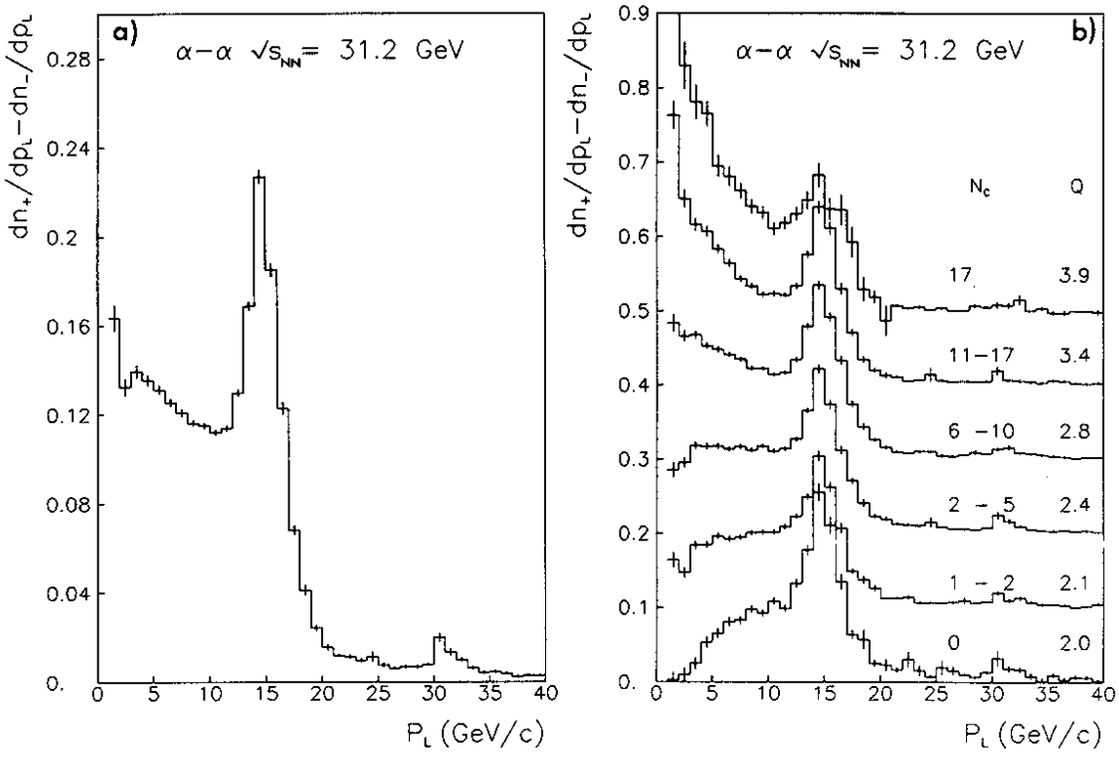
a)
α−α √s_NN= 31.2 GeV
dn+/dpL−dn−/dpL
PL (GeV/c)
b)
α−α √s_NN= 31.2 GeV
Nc
Q
17
3.9
11−17
3.4
6 −10
2.8
2 − 5
2.4
1 − 2
2.1
0
2.0
dn+/dpL−dn−/dpL
PL (GeV/c)

Fig. 9

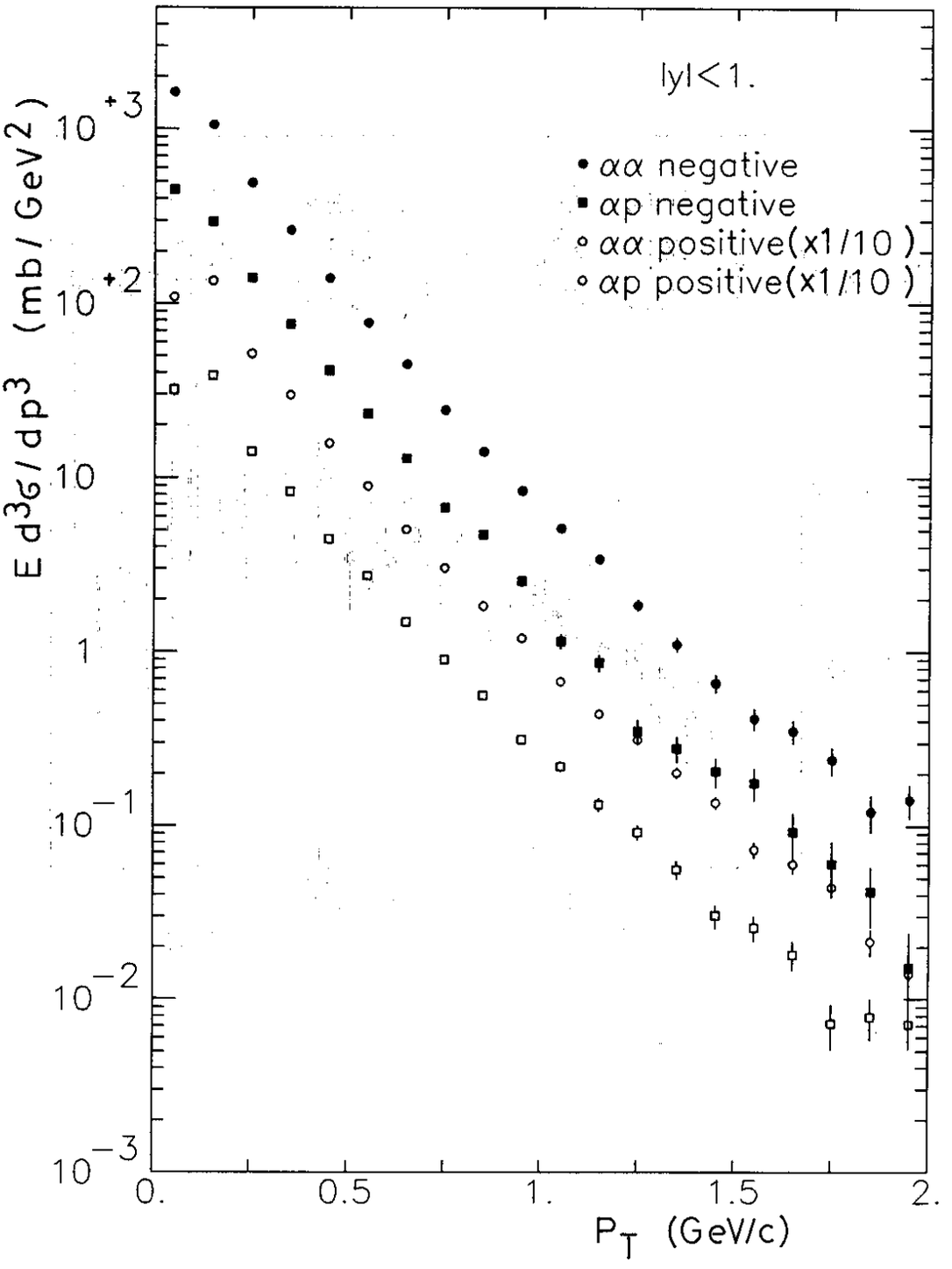
|y|<1.
• αα negative
▪ αp negative
◦ αα positive(x1/10)
◦ αp positive(x1/10)
E d³σ/ dp³ (mb/ GeV²)
10⁺³
10⁺²
10
1
10⁻¹
10⁻²
10⁻³
0.
0.5
1.
1.5
2.
P_T (GeV/c)

Fig. 10

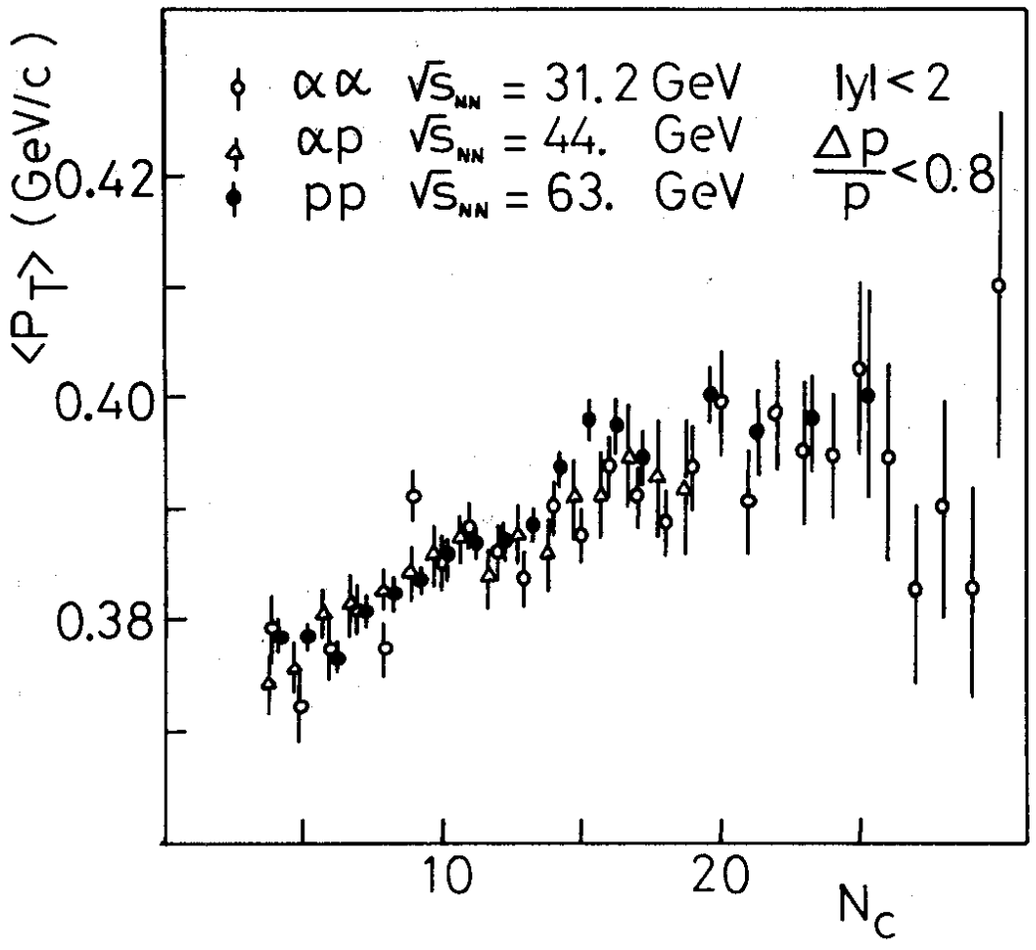
αα √s_NN = 31.2 GeV
αp √s_NN = 44. GeV
pp √s_NN = 63. GeV
|y|<2
Δp/p<0.8
<P_T> (GeV/c)
0.42
0.40
0.38
10
20
N_C

Fig. 11

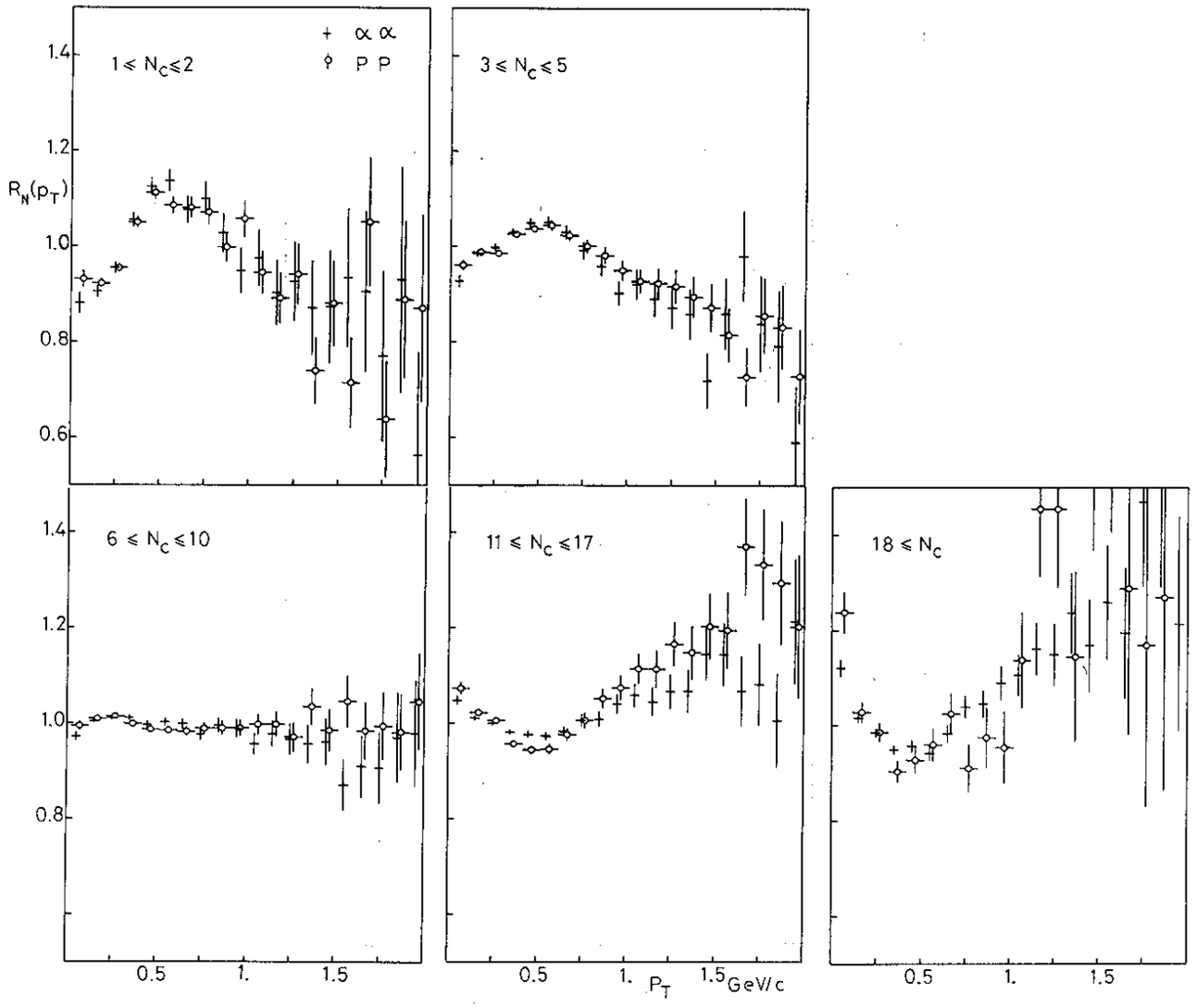

Fig. 12

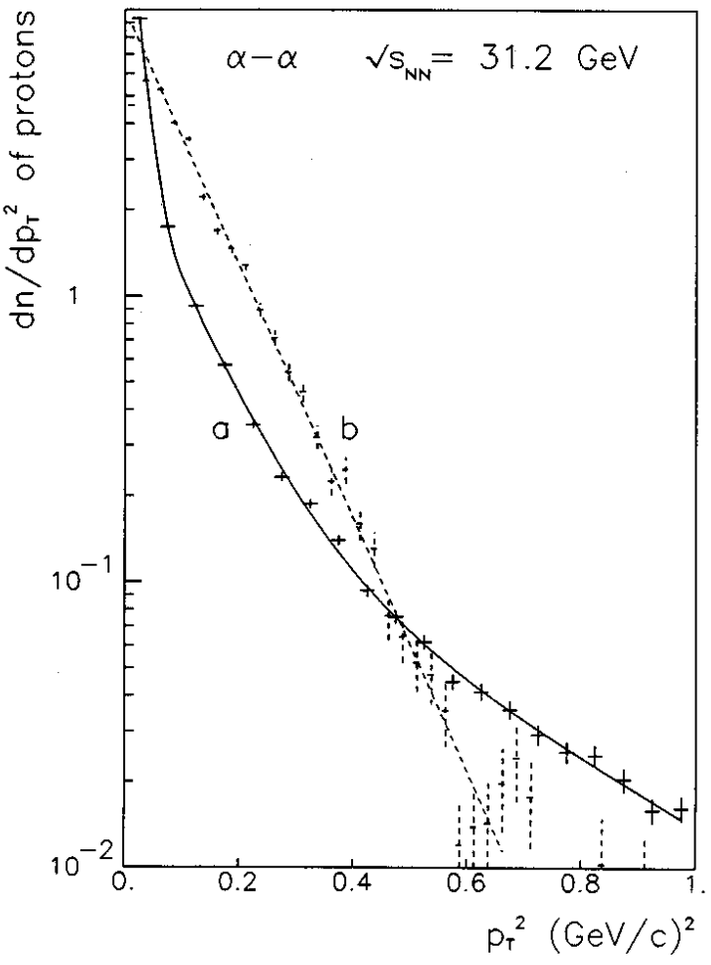
α−α √s_NN= 31.2 GeV
dn/dp_T^2 of protons
1
10^-1
10^-2
a
b
0.
0.2
0.4
0.6
0.8
1.
p_T^2 (GeV/c)^2

Fig. 13